remote sensing

MDPI

Article

Characterizing Urban Fabric Properties and Their Thermal Effect Using QuickBird Image and Landsat 8 Thermal Infrared (TIR) Data: The Case of Downtown Shanghai, China

Hao Zhang [1,*], Xing-Min Jing [1], Jia-Yu Chen [1], Juan-Juan Li [2] and Ben Schwegler [3]

[1] Department of Environmental Science and Engineering, Fudan University, 220 Handan Road, Shanghai 200433, China; 13210740025@fudan.edu.cn (X.-M.J.); 14210740041@fudan.edu.cn (J.-Y.C.)
[2] Disney Research China, The Walt Disney Company (China) Limited, 624 West Jianguo Road, Shanghai 200031, China; Joyce.Li@disney.com
[3] Department of Civil and Environmental Engineering, Stanford University, Stanford, CA 94305, USA; ben.schwegler@stanford.edu
* Correspondence: zhokzhok@163.com or zhanghao_fdu@fudan.edu.cn; Tel.: +86-139-1704-5425

Academic Editors: Benjamin Bechtel, Iphigenia Keramitsoglou, Simone Kotthaus, James A. Voogt, Klemen Zakšek, Richard Müller and Prasad S. Thenkabail
Received: 31 March 2016; Accepted: 20 June 2016; Published: 24 June 2016

Abstract: The combined usage of high-resolution satellite images and thermal infrared (TIR) data helps understanding the thermal effect of urban fabric properties and the mechanism of urban heat island (UHI) formation. In this study, three typical urban functional zones (UFZs) of downtown Shanghai were chosen for quantifying the relationship between fine-scale urban fabric properties and their thermal effect. Nine land surfaces and 146 aggregated land parcels extracted from a QuickBird image (dated 14 April 2014) were used to characterize urban fabric properties. The thermal effect was deduced from land surface temperature (LST), intra-UHI intensity, blackbody flux density (BBFD) and blackbody flux (BBF). The net BBF was retrieved from the Landsat 8 TIR band 10 dated 13 August 2013, and 28 May 2014. The products were resampled to fine resolution using a geospatial sharpening approach and further validated. The results show that: (1) On the UFZ level, there is a significant thermal differential among land surfaces. Water, well-vegetated land, high-rises with light color and high-rises with glass curtain walls exhibited relatively low LST, UHI intensity and BBFD. In contrast, mobile homes with light steel roofs, low buildings with bituminous roofs, asphalt roads and composite material pavements showed inverse trends for LST, UHI intensity, and BBFD; (2) It was found that parcel-based per ha net BBF, which offsets the "size-effect" among parcels, is more reasonable and comparable when quantifying excess surface flux emitted by the parcels; (3) When examining the relationship between parcel-level land surfaces and per ha BBF, a partial least squares (PLS) regression model showed that buildings and asphalt roads are major contributors to parcel-based per ha BBF, followed by other impervious surfaces. In contrast, vegetated land and water contribute with a much lower per ha net BBF to parcel warming.

Keywords: urban fabric; urban heat island; thermal effect; Shanghai; China

1. Introduction

To date, intensive human activities and anthropogenic climate change occurring across local, regional, and global scales have increasingly attracted concern [1–3]. Given the ongoing trends in global warming and over half of the world's population living in urban areas [4], urban dwellers in low and middle latitude regions will be subject to increasing thermal stress during summer. The urban heat

island (UHI) effect has therefore been a hot topic linking anthropogenic climate change and human health risks [5–8], energy consumption and carbon emission [9] as well as urban adaption to climate change [10].

Since the 1970s, satellite-based thermal remote sensing has been an important approach for characterization of the impact of local and regional climate change induced by intensive human activities, in particular modification of urban climate [11–13]. Recently, satellite thermal infrared (TIR) data, including HCMM, MODIS, Landsat TM/ETM+ and ASTER imagery, have been widely used to detect surface UHIs and depict spatial patterns of the urban thermal environment with varied resolutions and accuracies [14–16] due to their advantageous spatial coverage and temporal repetition. High-resolution TIR data, such as Landsat ETM+ (60 m) and ASTER (90 m) TIR data, were used with downscaling methods to sharpen coarse-resolution (more than 100 m) land surface temperature (LST) data to produce finer LST maps and thus enhance their application in regional thermal monitoring [17–19]. Unfortunately, existing downscaling algorithms, which were developed for sharpening images over rural and natural areas, have large errors when applied in urban areas [20]. Moreover, aforementioned high-resolution TIR data (60–90 m) are still too coarse to characterize fine-scale thermal effects of urban fabrics. Urban fabric properties represent developed parcels with buildings, vegetation and water and are used to determine fine-scale radiative balance and heat storage capacity, which are closely related to UHI formation [21,22]. Thus, high- or very high-resolution LST products (~m) are required for this research field. Several enhanced sharpening methods, which combine high-resolution satellite images and thermal infrared (TIR) data, have been developed for the production of high- or very high-resolution LST products [23,24]. However, applications of such enhanced LST products indicating fine-scale urban fabric properties and their thermal effect are still very scarce. Consequently, our understanding of the relationship between urban fabrics properties and mechanism of UHI formation is limited. In fact, detailed knowledge of the relationship between urban fabric properties and the mechanism of UHI formation is fundamental for the design of strategies to mitigate the UHI effect, improve human comfort, reduce building energy consumption and curtail carbon emissions.

This study aims to quantify the relationship between fine-scale urban fabric properties and their thermal effect using an integrated approach of remote sensing, spatial analysis, and statistical analysis. We hope to provide a practical approach for understanding the thermal effect of urban fabric via fine-resolution indicators, which will help mitigate UHI effects in populated megacities such as Shanghai and further enhance urban adaptability to climate change.

2. Study Area

The study area consists of three typical urban functional zones (UFZs) of downtown Shanghai, including the urban center, the Xujiahui sub-center, and a mixture of residence and campus (see Figure 1). A description of the three UFZs is shown in Table 1.

Table 1. Description of the three UFZs.

UFZ	Description
Mixture of residence and campus	This UFZ is located in the Hongkou district. It mainly consists of the Tongji University south campus, Peace Park, recreational landscaping, residential areas, and dense transport lines. It covers an area of 2.00 km^2 with a population density of approximately 35,698 people per km^2 [25].
Urban center	This UFZ is located in the Huangpu district. It mainly consists of the Shanghai municipal government, historical museum, great theater, the Nanjing road commercial and business area, bituminous streets, parks and recreational landscaping, residential areas, and dense transport lines. It covers an area of 5.97 km^2 with a population density of approximately 33,333 people per km^2 [25].
Xujiahui sub-center	This UFZ is located in the Xuhui district. It mainly consists of the Xujiahui commercial and business area, bituminous streets, Xujiahui Park, Hengshan Park, Song Ching-ling Mausoleum, recreational landscaping, residential areas, and dense transport lines. It covers an area of 2.58 km^2 with a population density of approximately 20,265 people per km^2 [25].

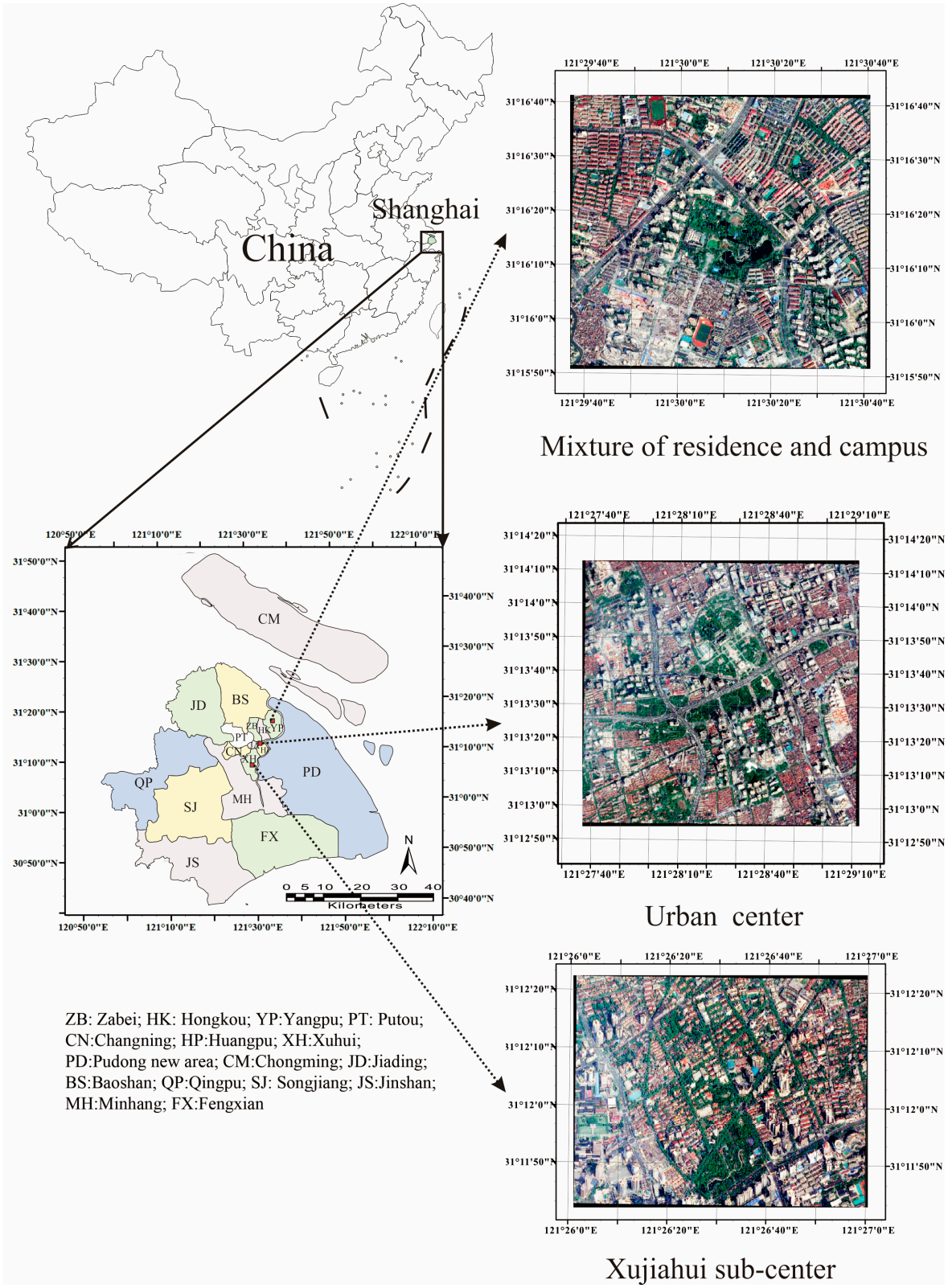

Figure 1. Location of the study area.

3. Materials and Methods

3.1. Satellite Data

In this study, three pan-sharpened QuickBird images (resolution 0.61 m at nadir) dated 14 April 2014 were used for mapping fine-scale land surfaces, which was further used for correction of emissivity values for land surfaces. The Landsat 8 TIR band data acquired on 13 August 2013 and 28 May 2014 were used for retrieval of land surface temperature (LST), intra-UHI intensity, blackbody/sensible heat flux density (BBFD), blackbody/sensible heat flux (BBF), and net BBF. Table 2 lists the descriptive information on Landsat 8 TIR band and pan-sharpened QuickBird data.

Table 2. Satellite data used in this study [26,27].

Satellite	Acquisition Date	Path/Row	Spectral Bandwidth (μm)	Spatial Resolution (m)
Landsat 8	13 August 2013 28 May 2014	118/38	Band 1—Coastal aerosol: 0.43–0.45 Band 2—Blue: 0.45–0.51 Band 3—Green: 0.53–0.59 Band 4—Red: 0.64–0.67 Band 5—NIR: 0.85-0.88 Band 6—SWIR 1: 1.57–1.65 Band 7—SWIR 2: 2.11–2.29 Band 8—Panchromatic: 0.50–0.68 Band 9—Cirrus: 1.36–1.38 Band 10—TIR1: 10.60–11.19 Band 11—TIR2: 11.50–12.51	30 30 30 30 30 30 30 15 30 100 (30) 100 (30)
QuickBird	14 April 2014	-	Band 1—Blue: 0.430–0.545 Band 2—Green: 0.466–0.620 Band 3—Red: 0.590–0.710 Band 4—NIR: 0.715–0.918	2.44 (0.61)

Note: SWIR: shortwave infrared; NIR: Near Infrared; The Landsat TIR bands were originally acquired at 100 m resolution and officially distributed by NASA with resampled product (30 m). The pan-sharpened QuickBird composite image was resampled from 2.44 m to 0.61 m.

3.2. Methods

This section focuses on three aspects: (1) characterizing urban fabric properties with land surfaces and land parcels; (2) indicating the thermal effect of urban fabric properties with LST, UHI intensity, BBFD, BBF, and net BBF; and (3) quantifying the relationship between parcel-level net BBF and land surfaces. To clearly illustrate our research interests and goals, a technical flowchart describing preprocessing of remote sense data, classification, retrieval of LST, computation of UHI intensity and UHI magnitude is shown in Figure 2.

3.2.1. Preprocessing, Classification, and Post-Classification of QuickBird Image

The pan-sharpened QuickBird image (resolution 0.61 m) was used to map fine-scale land covers of the study area. With necessary preprocessing steps including atmospheric correction and georeference, the object-oriented classification of the QuickBird image was performed. Based on the knowledge from previous urban planning and in-situ investigations, nine land surfaces were classified (Table 3). The overall accuracy before manual correction is 80%. The land surfaces product was then manually corrected and validated in a field survey. Three group members independently tested the correction accuracy, which was determined to be 93%.

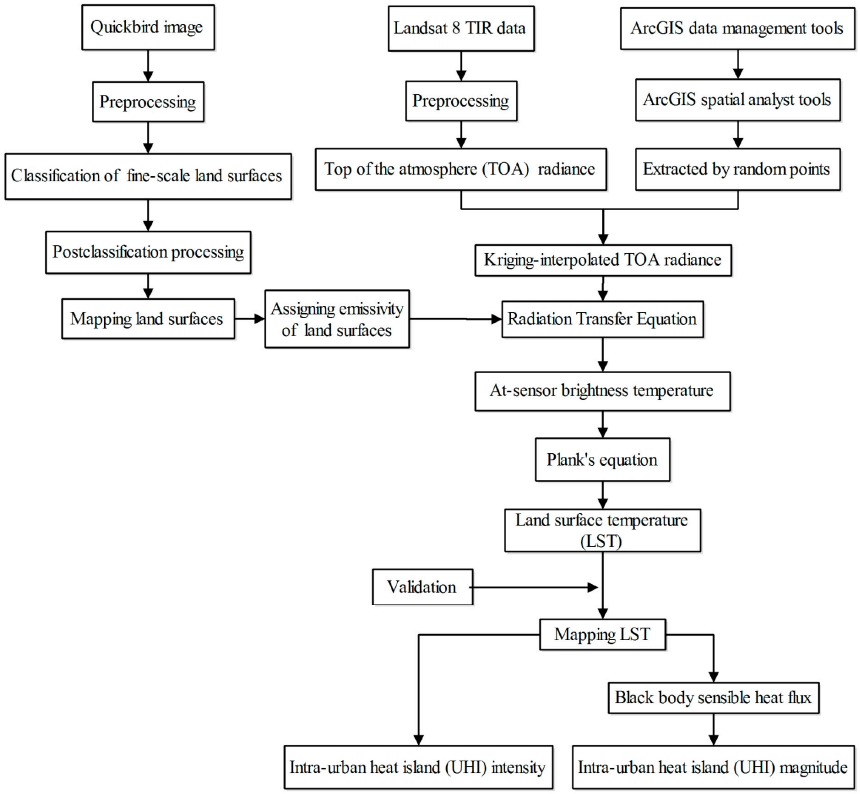

Figure 2. Technical flowchart for this study.

Table 3. Major land surfaces in this study.

Land Surface	Description
Water	Rivers, lakes, ponds, and dikes
Vegetation	Collection of trees, shrubs, and lawns including: (1) Evergreen and deciduous, broad-leaved and coniferous trees; (2) Forest nurseries, hedges, and ornamental plants; and (3) Open/enclosed playground and recreational landscaping with turfs
High-rise	This land surface consists of two categories including: (1) High-rise (8 stories or more, usually up to 30 stories) painted with white and light color or exterior wall was coated using light-colored materials; and (2) High-rise (8 stories or more, usually up to 30 stories) for commercial use, glass curtain wall coats
Low building	Old and low buildings (1–6 stories) and historical villas refurnished with bituminous roofs
Mobile home	Temporary home with light steel roof, which is usually set up for workers and guards at construction sites
Asphalt road	Traffic roads with asphalt concrete, bituminous streets
Land under construction/ for redevelopment	Enclosed land under construction or temporary vacant land with demolition of buildings
Composite material pavement	Sport tracks, tennis courts, and playgrounds with composite material pavement
The shaded area	Above-mentioned land surfaces shaded by neighboring higher objects, such as trees and buildings

3.2.2. Recognition of Typical Land Parcels

The complicated land surfaces in urban settings may cause difficulties when interpreting the relationship between fine-scale urban fabric properties and their thermal effect. Therefore, it is necessary to classify varying land surfaces into acceptable categories to clearly explain the differential

thermal effect of land surfaces and the mechanism of UHI effect formation. Given the massive population aggregation and land development intensity, land parcels are defined in this study as aggregated land units with regular shapes, such as residential community, business area, park and recreational landscaping, which are enclosed by traffic roads, walls and other things with regular shape. Three approaches were made to recognize typical land parcels of the study area. Firstly, with reference to commercial GIS shapefiles [28] and field survey, a series of polygons enclosing the land parcels was drawn and manually adjusted. Secondly, based on fine-scale land surfaces and building properties (including building height, story, age and density), a hierarchical clustering analysis with complete Euclidean distance was performed to subdivide these polygons into six groups. Thirdly, by carefully checking the result of the second step, some misclassifications of land parcels were corrected. Accordingly, the spatial extent of the polygons was manually adjusted. Finally, a total of 146 land parcels divided into six groups were recognized (Table 4).

Table 4. Description of typical land parcels in this study.

Land Parcel Type	Description
Type 1: Well-planned residential community	Well-planned low-density residential community with high buildings. Building density ranges from 25% to 35% with an average of 26%.
Type 2: Mixture of middle-density residential community and business area	Mixture of middle-density residential community and business area. Building density ranges from 27% to 51% with an average of 38.9%.
Type 3: Unplanned residential community	(1) High-density residential community with old and low buildings (2–3-story apartments), building density ranges from 50% to 88% with an average of 61%; (2) High-density residential community with old and low buildings (single-story houses or 3–6-story apartments), building density ranges from 46% to 66% with an average of 56%.
Type 4: Mixture of high-density residential community, public service and business area	Mixture of high-density residential community (low and old buildings) and business area. Building density ranges from 49% to 60% with an average of 53.9%.
Type 5: Land under construction/ for redevelopment	Enclosed land occupied by unfinished buildings or land under clearance (with building demolitions) for redevelopment.
Type 6: Park and recreational landscaping	Well-vegetated parks and recreational places. Building density ranges from 2% to 20% with an average of 11.1%.

3.2.3. Assignment of Emissivity of Fine-Scale Land Surface

Correction of land surface emissivity is very important for the retrieval of LST from TIR bands. Such a process is always subject to simplified emissivity of land surfaces and mixing effect of neighboring pixels. Herein, specific emissivity values were assigned to fine-scale land surfaces (Table 5). The estimated emissivity values for water and vegetation were 0.9925 and 0.95, respectively [29,30]. The emissivity values for other land surfaces were estimated according to the user guide of the UNI-T thermal camera [31].

Table 5. Assigned emissivity of land surfaces in this study.

Land Surface	Assigned Emissivity
Water	0.9925
Vegetation (tree, shrub and lawn)	0.95
High-rise building with light color	0.90
High-rise building with glass curtain wall	0.94
Low building with bituminous roof	0.85
Mobile home with light steel roof	0.66
Asphalt road	0.85
Land under construction/for development	0.83
Composite material pavement	0.92

3.2.4. Retrieval of Fine-Scale LST

Two Landsat 8 images acquired during clear days of hot summertime (13 August 2013, 2:27 a.m. GMT) and early summertime (28 May 2014, 2:24 a.m. GMT) were used for LST retrieval. As recommended, the TIR band 10 was used because band 11 is subject to higher uncertainty due to telescope stray light disturbance [26]. Because the coarse resolution of TIR data is not good enough for retrieving fine-scale LST, it is necessary to produce fine-scale TIR data. For this purpose, we applied the co-Kriging method. Considering the extent of our study area, at least 5000–10,000 random points were generated within the Landstat 8 TIR band 10 data layer covering the study area. These points were then interpolated to raster layers with the co-Kriging method. Furthermore, the coarse resolution of the LST product was resampled to fine-resolution (1 m, 3 m, 6 m, and 10 m). Pointwise checking of overlapped maps of LST and land covers showed that the 1-m resolution LST product visually provides more detailed information and better matches the fine-scale land cover. Compared with the 1-m resolution LST product, the 3–10 m LST maps exhibit more fluctuating LST values at some intersections of different land cover. Subsequently, the interpolated TIR data with 1-m resolution were used for retrieval of fine-scale LST with the following procedure.

Firstly, to perform calibration of TIR data, the quantized and calibrated standard product pixel values of interpolated TIR data were converted to at-sensor radiance or top of the atmospheric (TOA) radiance.

$$L_{sensor,\lambda} = M_L Q_{cal} + A_L \quad (1)$$

where $L_{sensor,\lambda}$ is TOA radiance, which is measured in Watts/($m^2 \cdot$ srad$\cdot$ μm), M_L is the band-specific multiplicative rescaling factor from the metadata, A_L is the band-specific additive rescaling factor from the metadata, and Q_{cal} is the quantized and calibrated standard product of pixel values [26].

Secondly, a generalized single channel method was applied for LST retrieval [32].

$$L_{sensor,\lambda} = [\varepsilon_\lambda B_\lambda (T_S) + (1 - \varepsilon_\lambda) L^{\downarrow}_{atm,\lambda}] \tau_\lambda + L^{\uparrow}_{atm,\lambda} \quad (2)$$

where $L_{sensor,\lambda}$ is TOA radiance, $B_\lambda(T_S)$ is the black body given by the Plank's law, T_S is the black body LST in Kelvin (K), ε_λ is the corrected emissivity of specific land surface, $L^{\downarrow}_{atm,\lambda}$ is the downwelling atmospheric radiance, $L^{\uparrow}_{atm,\lambda}$ is the upwelling atmospheric radiance, and τ_λ is the total atmospheric transmissivity between surface and sensor. $L^{\downarrow}_{atm,\lambda}$, $L^{\uparrow}_{atm,\lambda}$, and τ_λ are retrieved using the web-based Atmospheric Correction Tool [33]. Based on Equation (2), $B_\lambda(T_S)$ is calculated as follows.

Thirdly, *Ts* was computed as follows:

$$Ts = \frac{k_2}{\ln\left(1 + \frac{k_1}{B_\lambda(T_S)}\right)} \quad (3)$$

where k_2 and k_1 are band 10 thermal conversion constants, which can be found in the metadata file distributed by the USGS with the raw band data (k_1_constant_band_10 and k_2_constant_band_10) [26].

3.2.5. Validation of Fine-Scale LST

The comparison of the range of fine-scale *Ts* and original coarse *Ts* indicated significant offsets between them. Therefore, potential outliers were identified as follows [34],

$$\begin{cases} Outlier > UBV + 1.5 \times (Q_3 - Q_1) \\ Outlier < LBV - 1.5 \times (Q_3 - Q_1) \end{cases} \quad (4)$$

where *UBV* and *LBV* are upper and lower boundary values of the box plot, respectively. Q_3 is the third quartile, Q_1 is the first quartile, and $Q_3 - Q_1$ is the interquartile range. Three hundred random points were generated for each LST layer and land cover map, which were overlapped for pointwise checking

of extreme values falling within the assumed rejection intervals for outliers. Subsequently, the verified outliers were deleted to make sure the range of fine-scale *Ts* is in good agreement with that of the original coarse *Ts* (R^2 = 0.63, RMSE = 2.26 K). Finally, ranges of the corrected LST maps were rescaled to be consistent with those of the original coarse maps. Figure 3 shows an example illustrating before and after validation of the fine-scale LST map (13 August 2013) of the urban center UFZ. To avoid confusing cooling effect due to building's shading and vegetation's evapotranspiration, in this figure the shaded areas were marked black and excluded from the range of LST.

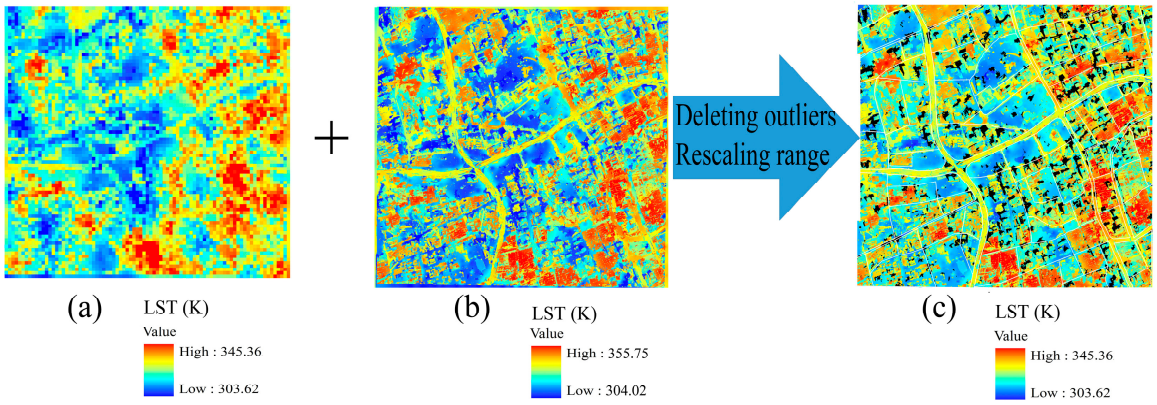

Figure 3. An example illustrating the before/after validation of fine-scale LSTs at the urban center UFZ: (**a**) Raw LST; (**b**) Biased LST before validation; and (**c**) LST after validation.

3.2.6. Measuring Intensity and Magnitude of Intra-UHI

In thermal remote sensing studies, both UHI intensity and magnitude are two widely used indicators to quantify the thermal effect of urban built environment. Usually, UHI intensity can be defined as the average LST difference between urban and rural areas. However, there is no available QuickBird image covering rural area, which makes it impossible to produce sharpened LST data for rural areas. Moreover, we focus on urban settings and their thermal effect in the context of built environment. Therefore, intra-UHI intensity rather than generalized UHI intensity was used in this study. Intra-UHI intensity was measured with the average LST difference between impervious surfaces (e.g., building, asphalt road and other impervious pavements) and cooling surfaces (vegetated land and water) within the downtown area.

Correspondingly, intra-UHI magnitude was measured using black body sensible heat flux (BBF) because of two reasons. First, it is a reasonable choice representing heating of the atmosphere by the urban land surface. Second, it bridges urban land surface thermal effect and energy demand for cooling [35]. Because BBF is area-dependent, it is calculated as follows in this study:

$$BBF_{\mathrm{i}} = \Phi_{BBFD} \times A_{\mathrm{i}} \tag{5}$$

where BBF_i is BBF (W) of the ith land parcel, A_i is area of the ith land parcel (m^2).

$$\Phi_{BBFD} = \int_{10.60\ \mu m}^{11.19\ \mu m} \frac{C_1}{\pi\lambda^5[\exp(\frac{C_2}{\lambda T})]} d\lambda \tag{6}$$

where Φ_{BBFD} is black body flux density ($W \cdot m^{-2}$), $C_1 = 3.7404 \times 10^8$ ($W \cdot \mu^4 \cdot m^{-2}$), $C_2 = 14387$, λ is TOA radiance, and T is LST in Kelvin (K).

Therefore, net BBF is calculated as follows:

$$Net\ \ BBF_i = BBF_i - BBF_C \tag{7}$$

where $Net\ BBF_i$ is net BBF of the ith land parcel and BBF_C is the average BBF of park and recreational landscaping with cooling surface [35].

However, given the fluctuation of specific parcel sizes and their contribution to excess surface flux emitted by the parcels, the converted per ha net BBF offsetting the "size-effect" is more reasonable and comparable between different land parcels. Therefore, per ha net BBF rather than net BBF was used to indicate parcel-specific contribution to excess surface flux.

3.2.7. Statistical Analysis

To quantify the potential relationship between parcel-level per ha net BBF and independent variables, a partial least squares regression (PLS) model containing five components was used to exclude potential co-linearity effects between independent variables. The PLS model is written as follows:

$$Y = \alpha + \beta_1 \times X_1 + \beta_2 \times X_2 + \beta_3 \times X_3 + \beta_4 \times X_4 + \beta_5 \times X_5 + \varepsilon \quad (8)$$

where Y is parcel-level per ha net BBF; α is a constant; β_1–β_5 are the associated coefficients of the regressive items; X_1–X_5 are percentages of reclassified land surfaces, including building, asphalt road, water, vegetation, and other land surfaces (composite material pavements and land under construction/land for redevelopment), respectively; and ε is the random error term. Moreover, the leave-one-out cross-validation method was used to select the optimal number of PLS factors included in the regression models [36,37]. Both the coefficient of determination (R^2) and the p value (0.01) were used to validate the performance of the PLS regression model. These statistical processes were performed using the commercial data processing system (DPS12.5) statistical package [38].

4. Results

4.1. UFZ-Level Land Surfaces and Their Thermal Effect

Figure 4 presents the overall spatial configuration of major land surfaces of the study area. Table 6 shows that there was remarkable variation in the percentages of UFZ-level land surfaces. When measured in individual land surfaces, the vegetation occupied the biggest share (24.2%–26.3%) of all land surfaces across three UFZs, followed by varying ranks of high-rise (17.0%–21.7%), low building (11.6%–23.2%) and asphalt road (13.6%–18.6%), which account for 55.0%–55.5% of impervious land surfaces across three UFZs. It is noted that, on average, water only accounts for the least share (1.19%) of all land surfaces. In summary, the spatial patterns of fine-scale land surfaces of three UFZs were generally characterized by dominant impervious land surfaces and fragmented pervious land surfaces (vegetation and water).

Table 6. Descriptive statistics of land surfaces in three UFZs.

Land Surface	UFZ		
	Mixture of Residence and Campus	Urban Center	Xujiahui Sub-Center
Vegetation	24.2%	25.7%	26.3%
Water	0.6%	1.6%	1.4%
High-rise	17.0%	21.7%	20.1%
Low building	23.2%	11.6%	21.4%
Mobile home	1.2%	1.4%	0.5%
Asphalt road	18.6%	23.6%	13.6%
Land under construction/for redevelopment	5.5%	2.8%	1.2%
Composite material pavement	0.0%	4.0%	1.4%
The shaded area	9.7%	7.7%	14.2%

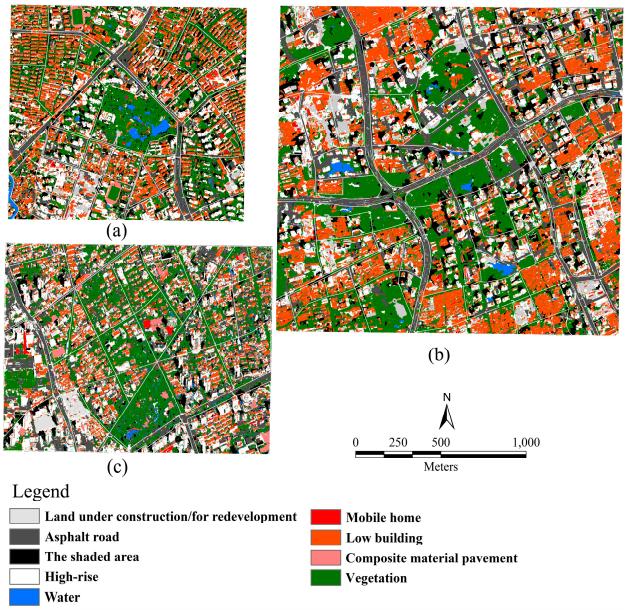

Figure 4. UFZ-level land surfaces at: (**a**) Mixture of residence and campus; (**b**) Urban center; and (**c**) Xujiahui sub-center.

Figures 5 and 6 show the overall pattern of LST in the study area for two dates. The range of LST varied remarkably for different TIR data acquisition dates. Water, well-vegetated land (e.g., People Park, mid Yan'an road Park, Huaihai Park, Taipingqiao Park, Peace Park and Xujiahui Park), high-rise with light color and high-rise with glass curtain wall exhibit a relatively low LST. However, mobile homes with light steel roofs, low buildings with bituminous roofs, asphalt roads and composite material pavements show relatively higher LST values. Figure 7 displays UHI intensity measured with the LST difference (mean $\pm$ standard deviation) between the cooling surfaces (water and vegetated land) and other land surfaces with warming surfaces. On the two dates, UHI intensity between the cooling surfaces and composite material pavement ranks the highest followed by mobile homes with light steel roofs, old and low buildings with bituminous roofs and asphalt roads. While UHI intensities between the cooling surfaces and light colored high-rise buildings with, land under construction or redevelopment and high-rise buildings with glass curtain walls are much lower.

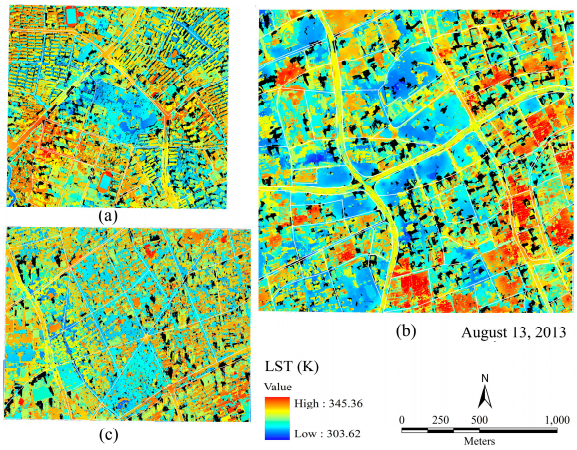

Figure 5. LST pattern of three UFZs (13 August 2013, 2:27 a.m. GMT): (**a**) Mixture of residence and campus; (**b**) Urban center; and (**c**) Xujiahui sub-center. Note: In this figure, the shaded areas were marked black and excluded from the range of LST.

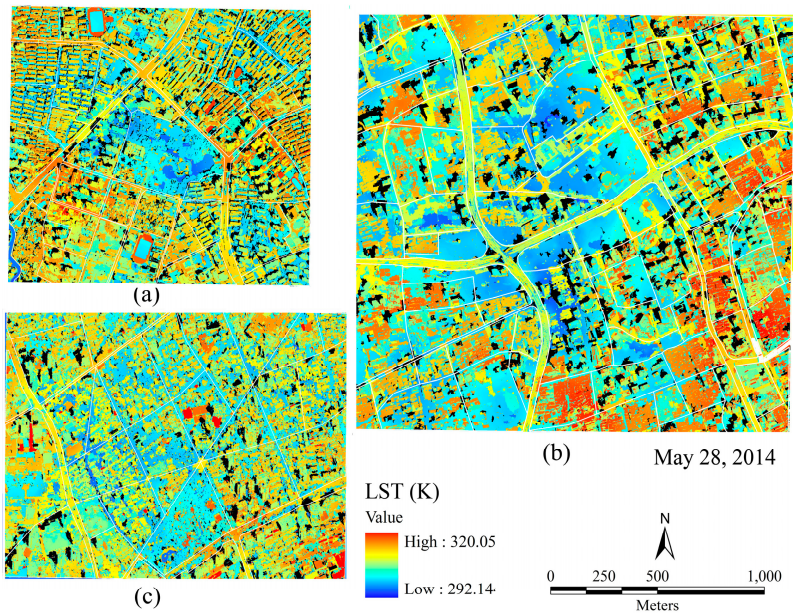

Figure 6. LST pattern of three UFZs (28 May 2014, 2:24 a.m. GMT): (**a**) Mixture of residence and campus; (**b**) Urban center; and (**c**) Xujiahui sub-center. Note: In this figure, the shaded areas were marked black and excluded from the range of LST.

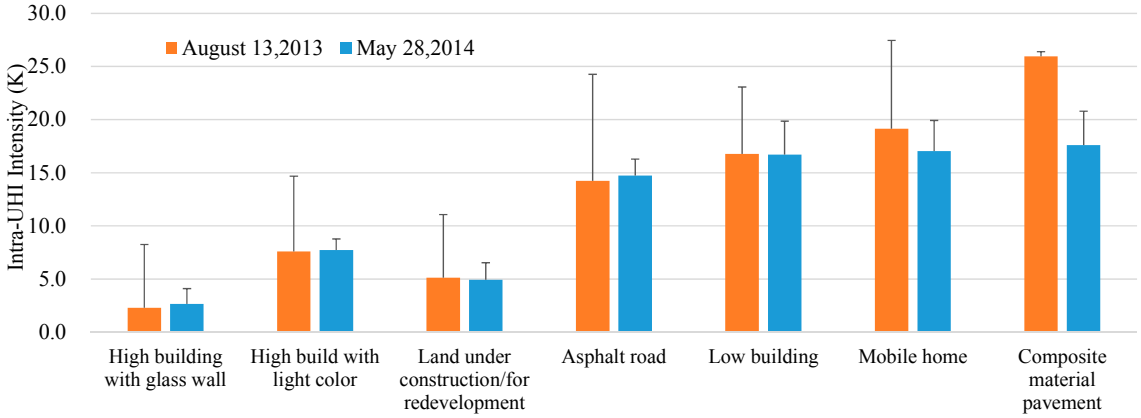

Figure 7. Variation of UHI intensity (mean ± standard deviation) between the cooling surfaces and the other land surfaces.

Figures 8 and 9 show the overall pattern of BBFD during hot summertime day (13 August 2013) and early summertime day (28 May 2014) in the study area. Figure 10 further displays the variation of average BBFD associated with specific land surfaces. Water, well-vegetated land, high-rise with light color and high-rise with glass curtain wall exhibit relative low BBFDs, compared with mobile home with light steel roof, low building with bituminous roof, composite material pavement and asphalt road.

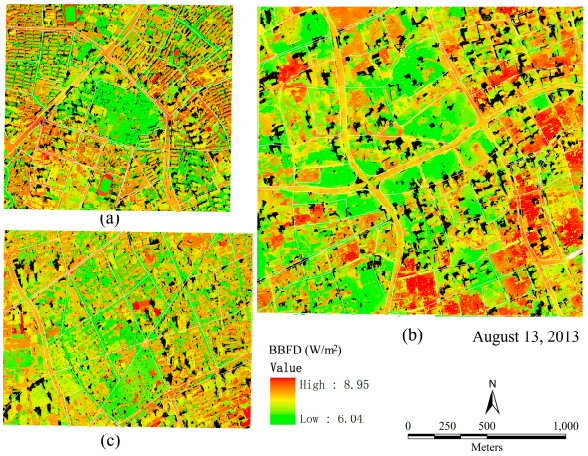

Figure 8. Retrieved BBFD (W/m^2) (13 August 2013, 2:27 a.m. GMT): (**a**) Mixture of residence and campus; (**b**) Urban center; and (**c**) Xujiahui sub-center. Note: In this figure, the shaded areas were marked black and excluded from the range of BBFD.

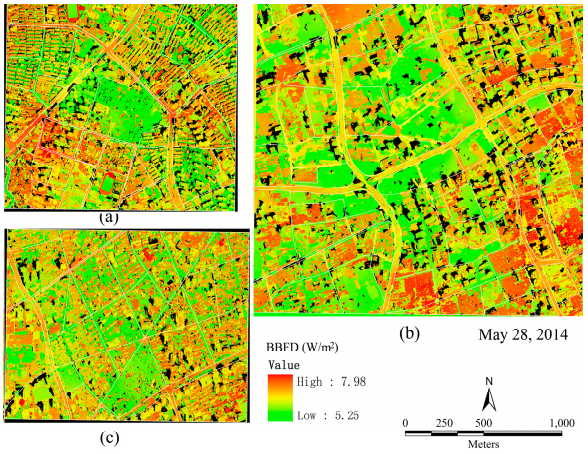

Figure 9. Retrieved BBFD (W/m^2) (28 May 2014, 2:24 a.m. GMT): (**a**) Mixture of residence and campus; (**b**) Urban center; and (**c**) Xujiahui sub-center. Note: In this figure, the shaded areas were marked black and excluded from the range of BBFD.

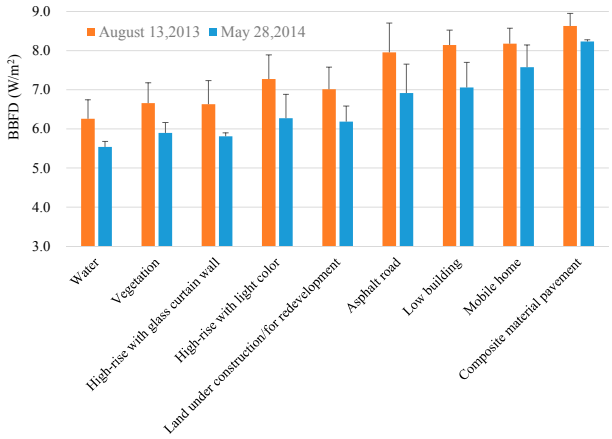

Figure 10. Retrieved BBFD (Mean $\pm$ standard deviation) associated with land surfaces. Note: in this figure the shaded areas were excluded.

4.2. Land Parcel Types and Their Thermal Effect

Table 7 shows six typical land parcel types and their percentages of the study area. Type 2 ranks first and Type 6 ranks second followed by Types 4, 1 and 3, with nearly even intervals. Type 5 occupies the lowest percentage. A description of land parcel types and their percentages at UFZ level is given in Table 8.

Table 7. Typical land parcel types and their percentages.

Land Parcel Type	Percentage
Type 1: Well-planned residential community	11.25%
Type 2: Mixture of middle-density residential community and business area	34.44%
Type 3: Unplanned residential community	8.76%
Type 4: Mixture of high-density residential community, public service and business area	14.21%
Type 5: Land under construction/for redevelopment	3.87%
Type 6: Park and recreational landscaping	27.47%

Table 8. Description of land parcel types and their percentages at UFZ level.

UFZ	Description
Urban center	FID for the land parcels numbered 2–77 in which parcel areas range from 1.47 to 21.87 ha with an average of 7.36 ha. Parcel Types 1, 2, 3, 4, 5 and 6 account for 11.27%, 26.76%, 19.72%, 22.54%, 7.04% and 12.58%, respectively.
Xujiahui sub-center	FID for the land parcels numbered 2–31 in which parcel areas range from 0.82 to 14.61 ha with an average of 5.81 ha. Parcel Types 1, 2, 3, 4, 5 and 6 account for 20.69%, 51.72%, 6.90%, 10.34%, 3.45% and 6.90%, respectively.
Mixture of residence and campus	FID for the land parcels numbered 2–41 in which parcel area ranges from 1.28 to 19.63 ha with an average of 5.64 ha. Parcel Types 1, 2, 3, 4, 5 and 6 account for 15.79%, 60.53%, 10.53%, 0.00%, 7.89% and 5.26%, respectively.

Note: FID means the feather's ID of each specific polygon of the UFZs, which was automatically assigned in ESRI ArcGIS software.

Figures 11 and 12 show the overall pattern of retrieved per ha net BBFs of the study area. A remarkable temporal variation of parcel-specific net BBFs can be observed on two dates. As an example, a generally much higher parcel-specific per ha net BBF and wider range (0.07–17.92 kW) was determined for 13 August 2013. Land parcels characterized with park and recreational landscaping, including Peace Park (numbered 22) of the mixture of residence and campus UFZ, People Park (numbered 62), Mid-Yan'an road Park (numbered 28, 35, 36, 39, and 45) of the urban center UFZ, Xujiahui Park (numbered 10) and Hengshan Park (numbered 15) of the Xujiahui sub-urban center UFZ always exhibited the lowest per ha net BBFs for the two dates (on average 2.37 kW on 13 August 2013 and 1.86 kW on 28 May 2014). In contrast, unplanned parcels numbered 18 and 19 of the mixture of residence and campus UFZ, parcels numbered 7, 8, 17 and 26 of the urban center UFZ and parcels numbered 7 and 13 of the Xujiahui sub-center UFZ exhibited the highest per ha net BBFs on the two dates (on average 12.23 kW on 13 August 2013 and 9.26 kW on 28 May 2014). Extreme low and high ranges for parcel-level per ha BBFs on 13 August 2013, were 0.18–4.88 kW and 6.76–15.66 kW, respectively. Extreme low and high ranges for parcel-level per ha BBFs on 28 May 2014, were 0.09–3.54 kW and 3.64–12.48 kW, respectively. This can be explained with seasonal variation of weather conditions.

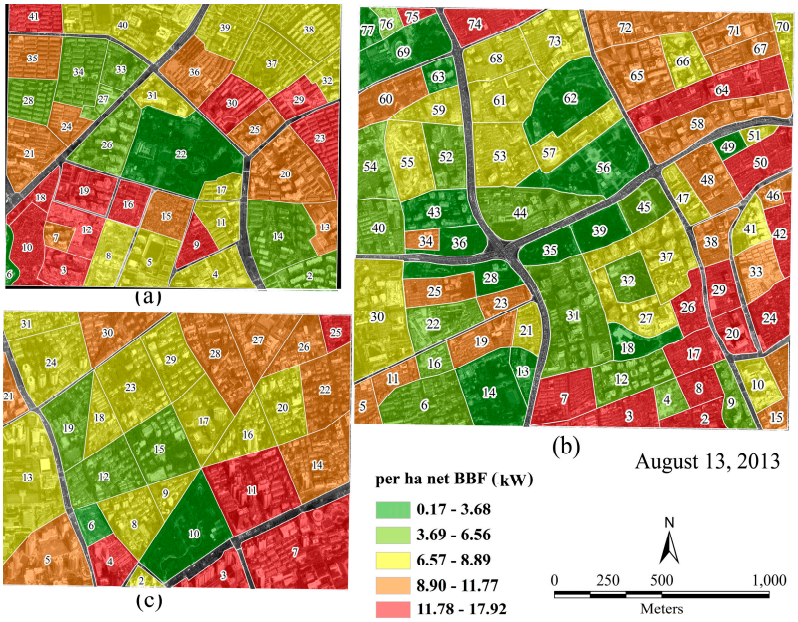

Figure 11. Retrieved per ha net BBF (13 August 2013, 2:27 a.m. GMT): (**a**) Mixture of residence and campus; (**b**) Urban center; and (**c**) Xujiahui sub-center. Note: In this figure, the shaded areas were marked black and excluded from the range of per ha net BBF; and each land parcel was enclosed by the numbered white polygon.

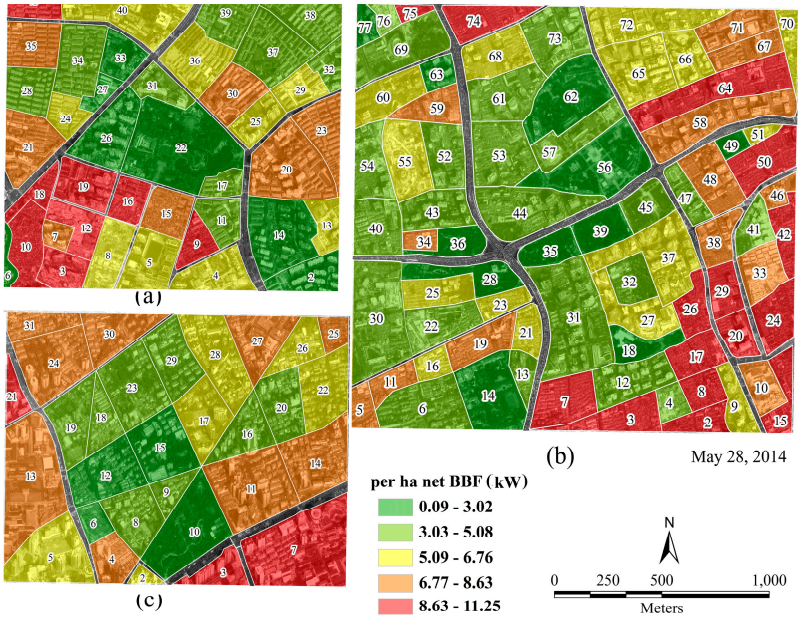

Figure 12. Retrieved per ha net BBF (28 May 2014, 2:24 a.m. GMT): (**a**) Mixture of residence and campus; (**b**) Urban center; and (**c**) Xujiahui sub-center. Note: In this figure, the shaded areas were marked black and excluded from the range of per ha net BBF; and each land parcel was enclosed by the numbered white polygon.

Furthermore, Figure 13 generally shows remarkable variation of per ha net BBFs (mean ± standard deviation) of six land parcels on the two dates. During the hot summer day (13 August 2013) all of the land parcels contributed higher per ha net BBFs than during the early summer day. On 13 August 2013, the Type 3 parcel exhibited the highest per ha net BBF and the Type 4 parcel exhibited the second

highest per ha net BBF, followed by Types 2, 5 and 1. Not surprisingly, Type 6 exhibited the lowest per ha net BBF. On 28 March 2014, the overall ranks of parcel-level per net BBF were similar to that on 13 August 2013, with the exception of the Type 4 parcel. To summarize, the parcel of Type 3, which is characterized by an unplanned residential community, contributed the highest per ha net BBF to parcel warming. The parcels of Types 2, 3, 4, and 5 were also major contributors resulting in parcel warming measured with per ha net BBF. In contrast, the parcel of Type 1 exhibited the lowest per ha net BBF level among impervious landscaping, indicating such a land parcel may help decrease excessive heat flux and potentially mitigate thermal stress of urban built environment.

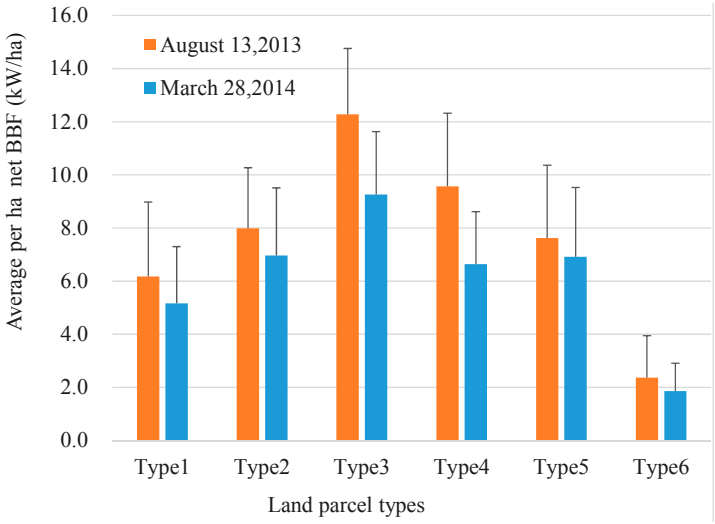

Figure 13. Average per ha net BBF (mean ± standard deviation) associated with land parcels of the study area.

4.3. Relationship between Parcel-Level Land Surfaces and Per ha Net BBF

The PLS regression models in Table 9 indicate that there exists a significant positive correlation between per ha net BBF and parcel land surfaces. The five-component models explain 66.0% and 68.0% of the variance in the predictors, respectively. The B-coefficients indicate the importance of each predictor in the regression models, showing that the buildings and asphalt roads are major contributors to per ha BBF, followed by others (composite material pavements and land under construction/land for redevelopment). In contrast, vegetation and water exhibit relatively low LST. Thus, given their minority in B-coefficients, they contribute much less per ha BBF to parcel warming.

Table 9. PLS regression models depicting the relationship between parcel-level land surfaces and per ha net BBF.

Independent Variable	13 August 2005		28 May 2014	
	B-Coefficient	**Summary Statistics**	**B-Coefficient**	**Summary Statistics**
Constant	−5.26 **		−4.20 **	
Building (%)	19.27 **		18.12 **	
Asphalt road (%)	16.79 **		15.78 **	
Water (%)	3.33 **		2.22 **	
Vegetation (%)	3.86 **		2.89 **	
The others (%)	8.98 **		7.44 **	
		Adjusted R^2: 0.66 ** F-statistic: 50.29 **		Adjusted R^2: 0.68 ** F-statistic: 54.75 **

Note: ** significant at *p*-level 0.01.

5. Discussion

5.1. Implications for Mitigating the UHI Effect

In addition to prevailing meteorological conditions across local- and meso-scales, urban fabric properties play the key role in formation of the UHI effect via complicated processes such as biophysical features of the land surfaces, building layout and wind corridor, landscape heterogeneity, energy consumption and anthropogenic heat emission [12,39–45]. In this study, we presented the differential thermal effect of urban fabric properties, i.e., LST, UHI intensity and BBFD associated with varying land surfaces at UFZ level. We also presented the differential thermal effect of parcel-level net BBF and per ha net BBF associated with typical land parcel types, which reflects parcel warming potential and UHI magnitude. Based on our findings and previous studies on mitigation of the UHI effect [17,46,47], we discussed observations and countermeasures, which should be beneficial for mitigating the UHI effect in downtown Shanghai and other megacities.

5.1.1. Reducing Impervious Surface Area

In practice, enhancing urban green spaces and water-covered areas (e.g., lake, pond, dike, etc.) is an effective way to reduce urban impervious surface area. Unfortunately, there is very limited space for new water-covered area in downtown Shanghai. Numerous creeks and channels disappeared over the past 50 years when this city rapidly expanded [48]. Alternatively, enhancing the urban green coverage ratio may be more practical. Since the 1990s, Shanghai has been a rapidly greening metropolis. Many new green spaces emerged, in particular, the Taipingqiao Park, mid-Yan'an road Park, the People Square, Century Park, the outer-ring greenbelt and numerous vest-pocket parks, which enhance the spatial configuration of green landscape in an urban area. As a result, the present green coverage ratio in downtown Shanghai is 38.4%, approximately 3.10-fold of that in 1990 [49]. However, according to our analysis, the overall vegetated land accounts for approximately 25.37% of the three UFZs due to the uneven pattern of existing green spaces within downtown Shanghai. Consequently, compared with the overall green coverage ratio of downtown Shanghai, these three UFZs are subject to the UHI effect [9,50]. Moreover, rapid growth of urban population demands more land for urban development, which results in land scarcity for expanding urban green space. Given the extremely high costs of demolition and resettlement, it seems impractical to repeat construction of parks such as the mid-Yan'an road Park (23 ha), which was designed by the municipal government to improve urban center habitat quality and to mitigate the UHI effect [50]. It was firmly implemented by removing many state-owned enterprises, public institutions and 11,000 households at the cost of 2600 million RMB Yuan in 2000–2001. Therefore, green rooftop and vertical planting may be alternatives to enhance the green coverage ratio in these populated UFZs with deficiency of vegetation and thus enhance urban resilience to the UHI effect.

5.1.2. Enhancing Albedo of Urban Land Surfaces

Urban area often shows a lower albedo than surrounding rural area due to its dominant darker surfaces, which results in lower thermal emittance and increase in the amount of solar radiation absorbed [12]. Thus, increasing albedo of urban land surfaces has been another practical way for mitigation of UHI, including using retroreflective materials in urban canyons [51] and changing the conventional roofs to the highly reflective roofs with albedos close to 0.7–0.8 [52,53]. For example, compared with "unmanaged" soil moisture, well-managed green roofs with relatively abundant soil moisture will reduce the surface and near-surface UHIs to cool roofs with an albedo value of 0.7 [46]. Another study shows that increasing urban albedo by 0.1 might result in an average daytime air temperature depression of approximately 0.3–0.5 °C [47]. In this study, we did not measure the albedo of the land surfaces. However, we found that high-rise with light-color and high-rise with glass curtain wall exhibit relatively lower LST, UHI intensity and BBFD, compared with asphalt road, low and old buildings with bituminous roof and temporary homes with light steel roofs. Therefore, based

on our findings, we recommend the replacement of dark wall coatings and roofs with light-colors to effectively decrease the UHI effect.

5.1.3. Enhancing Parcel-Level Land Development Intensity

As shown in Section 4.2, the parcels of impervious landscaping contributed relatively higher net BBF per ha to parcel warming during a typical summer day (13 August 2013). It is noted that when measured with net BBF per ha, parcels of Types 3 and 4 are not significantly higher than that of Types 1, 2 and 5. However, given their higher building density and lower flat ratio in downtown Shanghai, we propose that optimized land parcel design involving decrease of building density, increase of green space and creating space for wind corridors should be considered to improve the thermal environment in future urban regeneration planning.

5.2. Limitation of This Study

This study has a few intrinsic shortcomings because of several factors. Firstly, Landsat TIR sensors are not specifically designed for fine-scale thermal remote sensing of urban built environment. The coarse resolution of the TIR band is not good at capturing and differentiating thermal signals between neighboring pixels, even the TIR band was visually enhanced using sharpening techniques; Secondly, 16-day revisiting intervals for Landsat TIR sensors covering the area of interest and cloud contamination limit the availability of images. Thus, two-date Landsat 8 TIR data used in this study can only partly capture and reflect the limited thermal signal of downtown Shanghai. Thirdly, the nighttime UHI effect is missing in this study because Landsat 8 TIR data only captures the daytime signal. There is another free platform known as HJ-1 B satellite, which produces both daytime and nighttime TIR data (300-m resolution) with revisiting intervals for 3–4 days. However, how to assimilate the different TIR data and visually sharpen it to help understanding the fine-scale UHI effect is still a great challenge; Finally, in this study, a potential problem may arise due to the mismatched acquisition dates of QuickBird and Landsat 8 TIR data. For instance, in different seasons the location and extent of the shaded areas may change. As a result, these changes may alter fine-scale LST pattern associated with the shaded areas. Therefore, in order to fix the potential mismatched problem, it is better to use high-resolution images and Landsat-8 TIR data acquired during the same or adjacent dates.

6. Conclusions

In this study, fine-scale urban fabric properties and their thermal effect in three typical UFZs of downtown Shanghai, China, were quantified using a pan-sharpened QuickBird high-resolution image and fine-scale TIR data retrieved from Landsat 8 band 10 data, which was sharpened with a geostatistical method. The results show that: (1) Impervious land surfaces dominate the twelve land surfaces of the study area. On UFZ level, water, well-vegetated land, high-rise with light color and high-rise with glass curtain wall exhibit relatively low LST, intra-UHI intensity and BBFD. In contrast, mobile homes with light steel roofs, low building with bituminous roof, asphalt road, and composite material pavement exhibit relatively high LST, intra-UHI intensity and BBFD; (2) On parcel level, based on analysis on per ha net BBF associated with land parcel types, it was found that, on average, parcel-based per ha net BBF, which offsets the "size-effect" among parcels, is more reasonable and comparable when quantifying excess surface flux emitted by the parcels and warming effect; (3) When examining the relationship between parcel-level land surfaces and parcel-based per ha BBF, the PLS regression models show that buildings and asphalt roads are major contributors to parcel-based per ha BBF, followed by others (composite material pavements and land under construction/for redevelopment). In contrast, vegetation and water contribute much lower per ha BBF to parcel warming and have a cooling effect when compared with the other land surfaces.

In summary, we hope that our case study benefits researchers, planners and decision-makers who are engaged in urban planning, land resource management, and urban thermal remote sensing.

Acknowledgments: This study is jointly financed by the Walt Disney Company (China) Limited (Project Agreement CA1402), Natural Scientific Foundation of China (No. 41171432), and Natural Scientific Foundation of Shanghai (No. 11ZR1401900). We are indebted to U.S. Department of the Interior and U.S. Geological Survey for providing the publically accessible Landsat 8 data via http://earthexplorer.usgs.gov/. Special thanks are also given to NASA's online service for Atmospheric Correction Parameter Calculator via http://atmcorr.gsfc.nasa.gov/.

Author Contributions: Hao Zhang, Juan-Juan Li, and Ben Schwegler designed the overall ideas for this study and got involved in workshops of this study. Hao Zhang wrote this manuscript. Hao Zhang, Xing-Min Jing, and Jia-Yu Chen performed thermal remote sensing and processed data analysis. Hao Zhang, Xing-Min Jing, Jia-Yu Chen and Juan-Juan Li carried out field survey. Ben Schwegler was responsible for native English editing and revision of academic opinions.

Conflicts of Interest: The authors declare no conflict of interest.

References

1. Grimmond, S. Urbanization and global environmental change: Local effects of urban warming. *Geogr. J.* **2007**, *173*, 83–88. [CrossRef]
2. McCarthy, M.P.; Best, M.J.; Betts, R.A. Climate change in cities due to global warming and urban effects. *Geophys. Res. Lett.* **2010**, *37*, L09705. [CrossRef]
3. Patz, J.A.; Campbell-Lendrum, D.; Holloway, T.; Foley, J.A. Impact of regional climate change on human health. *Nature* **2005**, *438*, 310–317. [CrossRef] [PubMed]
4. UN DESA's Population Division. 2014 revision of the World Urbanization Prospects. Available online: http://www.un.org/en/development/desa/publications/2014-revision-world-urbanization-prospects.html (accessed on 10 October 2015).
5. Jenerette, G.D.; Harlan, S.L.; Buyantuev, A.; Stefanov, W.L.; Declet-Barreto, J.; Ruddell, B.L.; Myint, S.E.; Kaplan, S.; Li, X. Micro-scale urban surface temperatures are related to land-cover features and residential heat related health impacts in Phoenix, AZ USA. *Landsc. Ecol.* **2015**. [CrossRef]
6. McMichael, A.J.; Woodruff, R.E.; Hales, S. Climate change and human health: Present and future risks. *Lancet* **2006**, *367*, 858–869. [CrossRef]
7. Stone, B.; Hess, J.J.; Frumkin, H. Urban form and extreme heat events: Are sprawling cities more vulnerable to climate change than compact cities? *Environ. Health Perspect.* **2010**, *118*, 1425–1428. [CrossRef] [PubMed]
8. Tan, J.; Zheng, Y.; Tang, X.; Guo, C.; Li, L.; Song, G. The urban heat island and its impact on heat waves and human health in Shanghai. *Int. J. Biometeorol.* **2010**, *54*, 75–84. [CrossRef] [PubMed]
9. Zhang, H.; Qi, Z.F.; Ye, X.Y.; Cai, Y.B.; Ma, W.C.; Chen, M.-N. Analysis of land use/land cover change, population shift, and their effects on spatiotemporal patterns of urban heat islands in metropolitan Shanghai, China. *Appl. Geogr.* **2013**, *44*, 121–133. [CrossRef]
10. Georgescu, M.; Morefield, P.E.; Bierwagenb, B.G.; Weaver, C.P. Urban adaptation can roll back warming of emerging megapolitan regions. *Proc. Natl. Acad. Sci. USA* **2013**, *111*, 2909–2914. [CrossRef] [PubMed]
11. Roth, M.; Oke, T.R.; Emery, W.J. Satellite-derived urban heat islands from 3 coastal cities and the utilization of such data in urban climatology. *Int. J. Remote Sens.* **1989**, *10*, 1699–1720. [CrossRef]
12. Taha, H. Urban climates and heat islands: Albedo, evapotranspiration and anthropogenic heat. *Energ. Build.* **1997**, *25*, 99–103. [CrossRef]
13. Voogt, J.A.; Oke, T.R. Thermal remote sensing of urbane climates. *Remote Sens. Environ.* **2003**, *86*, 370–384. [CrossRef]
14. Weng, Q. Thermal infrared remote sensing for urban climate and environmental studies: Methods, applications, and trends. *ISPRS J. Photogramm. Remote Sens.* **2009**, *64*, 335–344. [CrossRef]
15. Marina, S.; Constantinos, C. Daytime urban heat islands from Landsat ETM+ and Corine land cover data: An application to major cities in Greece. *Sol. Energy* **2007**, *81*, 358–368.
16. Onishi, A.; Cao, X.; Ito, T.; Shi, F.; Imura, H. Evaluating the potential for urban heat-island mitigation by greening parking lots. *Urban For. Urban Green.* **2010**, *9*, 323–332. [CrossRef]
17. Bechtel, B.; Zakšek, K.; Hoshyaripour, G. Downscaling land surface temperature in an urban area: A case study for Hamburg, Germany. *Remote Sens.* **2012**, *4*, 3184–3200. [CrossRef]
18. Weng, Q.; Fu, P.; Gao, F. Generating daily land surface temperature at Landsat resolution by fusing Landsat and MODIS data. *Remote Sens. Environ.* **2014**, *145*, 55–67. [CrossRef]

19. Zhan, Q.; Meng, F.; Xiao, Y. Exploring the relationships between land surface temperature, ground coverage ratio and building volume density in an urbanized environment. In Proceedings of the 36th International Symposium on Remote Sensing of Environment, Berlin, Germany, 11–15 May 2015.
20. Essaa, W.; van der Kwast, J.; Verbeirena, B.; Batelaan, O. Downscaling of thermal images over urban areas using the land surface temperature-impervious percentage relationship. *Int. J. Appl. Earth Obs. Geoinform.* **2013**, *23*, 95–108. [CrossRef]
21. Muhs, S.; Herold, H.; Meinel, G.; Burghardt, D.; Kretschmer, O. Automatic delineation of built-up area at urban block level from topographic maps. *Comput. Environ. Urban Syst.* **2016**, *58*, 71–84. [CrossRef]
22. Bernabe, A.; Musy, M.; Andrieu, H.; Calmet, I. Radiative properties of the urban fabric derived from surface form analysis: A simplified solar balance model. *Sol. Energy* **2015**, *122*, 156–168. [CrossRef]
23. Chen, X.; Li, W.; Chen, J.; Rao, Y.; Yamaguchi, Y. A Combination of TsHARP and thin plate spline interpolation for spatial sharpening of thermal imagery. *Remote Sens.* **2014**, *6*, 2845–2863. [CrossRef]
24. Deng, C.; Wu, C. Estimating very high resolution urban surface temperature using a spectral unmixing and thermal mixing approach. *Int. J. Appl. Earth Obs. Geoinform.* **2013**, *23*, 155–164. [CrossRef]
25. Shanghai Statistical Bureau, NBS Shanghai Survey Office. *Shanghai Yearbook-2015*; China Statistical Press: Beijing, China, 2015.
26. Department of the Interior, U.S. Geological Survey. *Landsat 8 (L8) Data Users Handbook*; Version 1.0; EROS: Sioux Falls, SD, USA, 2015.
27. DigitalGlobe, Inc. Information Products (Standard Imagery) Data Sheet. Available online: https://dg-cms-uploads-production.s3.amazonaws.com/uploads/document/file/21/StandardImagery_DS_10-14_forWeb.pdf (accessed on 28 December 2014).
28. Beijing Digital Space Technology Co., Ltd. *The Standard GIS-Based Altas of Shanghai*; Beijing Digital Space Technology Co., Ltd.: Beijing, China, 2015.
29. Artis, D.A.; Carnahan, W.H. Survey of emissivity variability in thermography of urban areas. *Remote Sens. Environ.* **1982**, *12*, 313–329. [CrossRef]
30. Nichol, J.E. High-resolution surface temperature patterns related to urban morphology in a tropical city: A satellite-based study. *J. Appl. Meteorol.* **1996**, *35*, 135–146. [CrossRef]
31. Uni-Trend Inc. *The UNI-T® User Guidance Version 1.08.14s*; Uni-Trend Inc.: Shenzhen, China, 2014.
32. Barsi, J.A.; Schott, J.R.; Hook, S.J.; Raqueno, N.G.; Markham, B.L.; Radocinski, R.G. Landsat-8 Thermal Infrared Sensor (TIRS) Vicarious Radiometric Calibration. *Remote Sens.* **2014**, *6*, 11607–11626. [CrossRef]
33. Jimenez-Munoz, J.C.; Sobrino, J.A. A generalized single channel method for retrieving land surface temperature from remote sensing data. *J. Geophys. Res.* **2003**, *108*. [CrossRef]
34. Barsi, J.A.; Schott, J.R.; Palluconi, F.D.; Hook, S.J. Validation of a Web-Based Atmospheric Correction Tool for Single Thermal Band Instruments. In Proceedings of the SPIE Conference on Earth Observing Systems, San Diego, CA, USA, 22 August 2005.
35. Frigge, M.; Hoaglin, D.C.; Boris, I. Some implementations of the boxplot. *Am. Stat.* **1989**, *43*, 50–54.
36. Stone, B.; Norman, J.M. Land use planning and surface heat island formation: A parcel-based radiation flux approach. *Atmos. Environ.* **2006**, *40*, 3561–3573. [CrossRef]
37. Geladi, P.; Kowalski, B.R. Partial least-squares regression: A tutorial. *Anal. Chim. Acta* **1986**, *185*, 1–17. [CrossRef]
38. Gao, H.-X. *Applied Statistical Methods and SAS*; Peking University Press: Beijing, China, 2001.
39. Tang, Q.-Y.; Zhang, C.-X. *Data Processing System-Experimental Design, Statistical Analysis, and Data Mining*, 2nd ed.; Science Press: Beijing, China, 2010.
40. Baldinelli, G.; Bonafoni, S.; Anniballe, R.; Presciutti, A. Spaceborne detection of roof and impervious surface albedo: Potentialities and comparison with airborne thermography measurements. *Sol. Energy* **2015**, *113*, 281–294. [CrossRef]
41. Buyantuyev, A.; Wu, J. Urban heat islands and landscape heterogeneity: Linking spatiotemporal variations in surface temperatures to land-cover and socioeconomic patterns. *Landsc. Ecol.* **2010**, *25*, 17–33. [CrossRef]
42. Jusuf, S.K.; Wong, N.H.; Hagen, E.; Anggoro, R.; Hong, Y. The influence of land use on the urban heat island in Singapore. *Habitat. Int.* **2007**, *31*, 232–242. [CrossRef]
43. Oke, T.R. The energetic basis of the urban heat-island. *Q. J. R. Meteorol. Soc.* **1982**, *108*, 1–24. [CrossRef]
44. Zhao, Q.; Myint, S.W.; Wentz, E.A.; Fan, C. Rooftop Surface Temperature Analysis in an urban residential environment. *Remote Sens.* **2015**, *7*, 12135–12159. [CrossRef]

45. Zhang, Y.; Balzter, H.; Zou, C.; Xu, H.; Tang, F. Characterizing bi-temporal patterns of land surface temperature using landscape metrics based on sub-pixel classifications from Landsat TM/ETM+. *Int. J. Appl. Earth Obs. Geoinform.* **2015**, *42*, 87–96. [CrossRef]
46. Li, D.; Elie, B.Z.; Oppenheimer, M. The effectiveness of cool and green roofs as urban heat island mitigation strategies. *Environ. Res. Lett.* **2014**, *9*, 1–16. [CrossRef]
47. Sailor, D.J.; Kalkstein, L.S.; Wong, E. The potential of urban heat island mitigation to alleviate heat-related mortality: Methodological overview and preliminary modeling results for Philadelphia. In Proceedings of the 4th Symposium on the Urban Environment, Norfolk, VA, USA, 4 May 2002; pp. 68–69.
48. Chen, J.; Yang, K.; Zhao, J.; Yuan, W.; Wu, J.-P. Variation of river system in center district of Shanghai and its impact factors during the last one hundred years. *Sci. Geogr. Sin.* **2007**, *27*, 85–91.
49. Zhou, H.M.; Zhou, C.H.; Ge, W.Q.; Ding, J.C. The surveying on thermal distribution in urban based on GIS and remote sensing. *Acta Geogr. Sin.* **2001**, *56*, 189–197.
50. Shanghai Administration of Urban Greening and Cityscape (SAUGC). Available online: http://lhsr.sh.gov.cn/sites/wuzhangai_lhsr/neirong.aspx?infid=e101578b-8c70-4f74-a337-fb667fba183e&ctgid=d83d5ce5-062b-4402-8c78-8673748804d3 (accessed on 10 January 2016).
51. Rossi, F.; Morini, E.; Castellani, B.; Nicolini, A.; Bonamente, E.; Anderini, E.; Cotana, F. Beneficial effects of retroreflective materials in urban canyons: Results from seasonal monitoring campaign. *J. Phys. Conf. Ser.* **2015**, *655*, 012012. [CrossRef]
52. Touchaei, A.G.; Akbari, H. The climate effects of increasing the albedo of roofs in a cold region. *Adv. Build. Energy Res.* **2013**, *7*, 186–191. [CrossRef]
53. Kolokotsa, D.; Santamouris, M.; Zerefos, S.C. Green and cool roofs' urban heat island mitigation potential in European climates for office buildings under free floating conditions. *Sol. Energy* **2013**, *95*, 118–130. [CrossRef]